undergone both DSC-MRI and PET studies within an eight-day interval (mean: 3 days). The protocol for this study was reviewed and approved by the Ethics Committee of the National Cerebral and Cardiovascular Center, Osaka, Japan.

2.3.2. DSC-MRI study. The DSC-MRI scan was based on T_2^*-weighted dynamic images, acquired on a 1.5 T MRI scanner (Magnetom Vision; Siemens Medical Systems, Erlangen, Germany), using a gradient-echo single-shot echo-planar imaging (EPI) sequence with the following parameters: echo time (TE), 60.73 ms; matrix, 128 × 128; field of view, 23 × 23 cm^2; and slice thickness, 4 mm. The repetition time (TR) was 0.66 s for 11 out of 14 patients, 2 s for two patients, and 1.1 s for one patient. The flip angle, number of frames, and number of slices for the subjects with TRs of 0.66, 2, and 1.1 s were, respectively, 60°, 90 and 5; 90°, 40 and 10; and 60°, 60 and 8. Slice positions were carefully selected, so that a region of the horizontal portion of the MCA passed through the imaging slices. A 0.05 mmol kg^{-1} (0.1 ml kg^{-1}) bolus of Gd-DTPA (Magnevist; Bayer Yakuhin, Ltd, Osaka, Japan) was injected through an antecubital vein at 4 ml s^{-1}, followed by 20 ml of saline flush at the same rate.

The dynamic MRI images were filtered using a 3 × 3 uniform smoothing kernel, as commonly performed in data processing for DSC-MRI (Østergaard *et al* 1996a, Ibaraki *et al* 2005). In general, the SNR of dynamic EPI images acquired in DSC-MRI is relatively low, and therefore the application of smoothing filter is common practice. Twenty ROIs were drawn manually on normal gray matter regions. The curves of the ROIs were converted into TCCs using (3) (Rosen *et al* 1990):

$$C(t) = -\frac{1}{\mathrm{TE}} \ln\left(\frac{S(t)}{S_0}\right), \tag{3}$$

where $S(t)$ is the observed signal intensity at time t and S_0 is the signal intensity before arrival of contrast agent. The AIF was then reconstructed as described in section 2.1 (TB-AIF). Another AIF was obtained by drawing an ROI manually in a region of the horizontal portion of the MCA in the unaffected hemisphere. The signal intensity in that ROI was converted into TCCs (Rosen *et al* 1990), and utilized directly as the AIF (VS-AIF).

CBF was calculated using both TB-AIFs and VS-AIFs as previously described (Smith *et al* 2000). The fitted curves were extrapolated up to 500 s, and deconvolved using singular value decomposition (SVD) with a block-circulant matrix (Wu *et al* 2003b). The cutoff level was set at 5% of the maximum singular value. CBF values from VS-AIF were scaled so that the CBF value in the normal white matter region was 22 ml/100 g/min (Østergaard *et al* 1996a).

To examine the repeatability of the tissue-based method, the same data analysis was carried out again at intervals of two weeks or longer.

2.3.3. PET study. For 10 out of 14 patients, quantitative CBF images were measured using a HEADTOM-IV PET scanner (Iida *et al* 1989) (Shimadzu, Kyoto, Japan) with a spatial resolution of 4.5 mm at FWHM in conjunction with the ^{15}O-labeled gas inhalation steady state technique (Hirano *et al* 1994). Correction for tissue attenuation was carried out with a transmission scan using an external ^{68}Ge–^{68}Ga rod source. A scan for the measurement of CBF was performed during continuous inhalation of ^{15}O-labeled carbon dioxide ($C^{15}O_2$). During these scans, several blood samples were obtained through a 22-gauge needle placed into an antecubital artery, in order to measure the arterial blood radioactivity concentration at steady state. For four patients, quantitative CBF images were measured using ^{15}O-water and PET. In these subjects, PET acquisition was carried out using an ECAT 47 PET scanner (Siemens-CTI,

Knoxville, USA) in 2D mode, following a previously described ^{15}O-water autoradiography protocol (Shidahara *et al* 2002). After a 600 s transmission scan, a dynamic scan consisting of 14 frames over a total 90 s period (12 × 5 s and 2 × 15 s) was initiated following intravenous administration of 1110 MBq $H_2{}^{15}O$. Arterial blood was withdrawn continuously during the PET scan from the brachial artery through a catheter using a syringe pump (Harvard Apparatus, model 901) at a rate of 2.0 ml min^{-1}. The radioactivity concentration in the blood was measured using a continuous input function monitor system (Kudomi *et al* 2003). The CBF parametric image was calculated using the ^{15}O-water autoradiography. Model parameters defined in the ^{15}O-water autoradiography were adjusted to provide consistent results with the steady-state technique. Details of the protocol are available in Shidahara *et al* (2002).

2.3.4. Data analysis. The PET-CBF image was registered to an EPI image acquired before arrival of the contrast agent, using the SPM99 statistical parametric mapping software (Wellcome Department of Neurology, London). ROIs were placed over cortical gray matter regions of the MCA territory in both hemispheres. Large-vessel voxels were removed from the ROIs by a previously described procedure (Carroll *et al* 2002). The hemispheric mean of CBF values in the ROIs obtained was calculated in the three CBF images (obtained by the tissue-based method (TB-CBF), the arterial voxel selection method (VS-CBF) and PET (PET-CBF)), followed by calculation of the ratio of CBF in the affected hemisphere relative to the unaffected hemisphere. Bland–Altman analysis (Bland and Altman 1986, 1999) was used to determine the agreement between TB-CBF and PET-CBF, and between VS-CBF and PET-CBF. All data are presented as mean ± 1 SD.

3. Results

3.1. Simulation study

Figure 2 shows the results of a simulation study demonstrating the effects of changes in the assumed model parameters of A, $K_e(1+\alpha)$ and (t_2-t_1) on the calculated CBF values and the relative CBF ratios. Increase in A, a parameter that describes the height of AIF, caused decrease in the calculated CBF (figure 2(a)), but was not dependent on the absolute CBF values (figure 2(b)). ±20% change in A corresponded to errors of approximately ±20% in calculated CBF. Increases in $K_e(1+\alpha)$ caused slight increase in calculated CBF (figure 2(c)). ±20% changes corresponded to errors of approximately ±15% in calculated CBF, and there was almost no CBF dependence (figure 2(d)). Increases in t_2-t_1 resulted in small decrease in calculated CBF (figure 2(e)). ±20% change in (t_2-t_1) caused approximately ±10% changes in calculated CBF, which showed only little dependence on the absolute CBF values (figure 2(f)).

Figure 3 shows the results of simulation study demonstrating effects of sampling period on the shape of estimated AIFs and calculated CBF values. Increase in sampling period had only little influence on the shape of the reconstructed AIF (figure 3(a)). As a result, the change in the calculated CBF values was less than ±6% compared with the CBF value at 0.1 s, and also showed only little dependence on the absolute CBF values (figures 3(b) and (c)).

Figure 4 shows the results of simulation study demonstrating the effects of an error in assumed CBV on the shape of the estimated AIFs and calculated CBF values. When the CBV of tissues selected for reconstructing AIF was higher than 4.0 ml/100 g, the height of the reconstructed AIF increased compared with the true AIF (figure 4(a)). On the other hand, when the CBV in the tissues was lower than 4.0 ml/100 g, the height decreased compared with the true AIF (figure 4(a)). The change in the calculated CBF reached 16% compared with

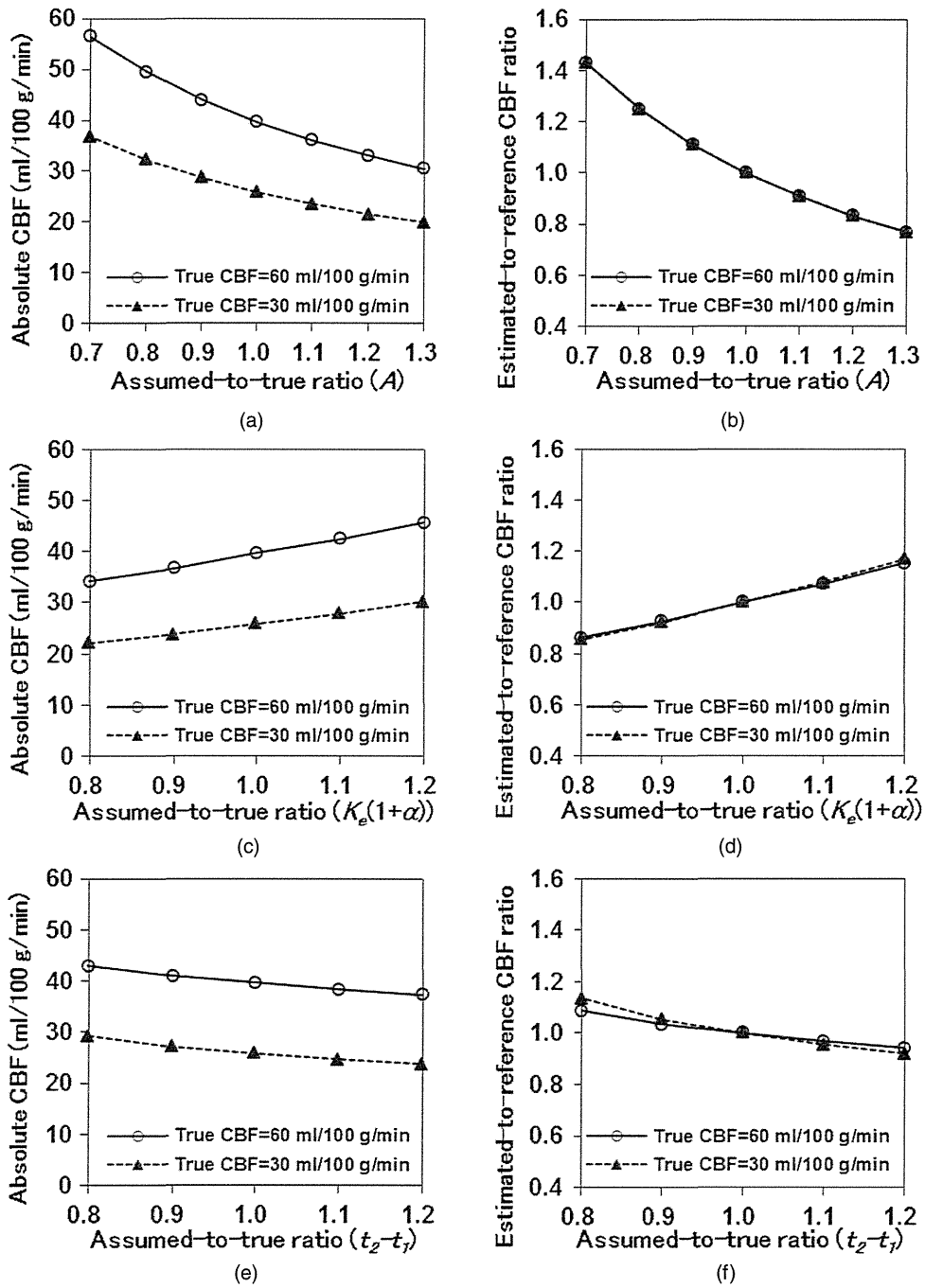

Figure 2. Effects of change in the parameters, which describe the shape of the arterial input function described in equation (1), on the estimated CBF values. (a, b) A, (c, d) $K_e(1+\alpha)$, (e, f) (t_2-t_1). Absolute CBF and relative CBF to a reference value at each condition are shown as a function of the parameter value. Assumed-to-true ratio is the ratio of the assumed parameter value to the true value, which is 1, obtained in a patient study. Estimated-to-reference ratio is the ratio of the calculated CBF value to the reference value obtained using the assumed-to-reference value of 1.0.

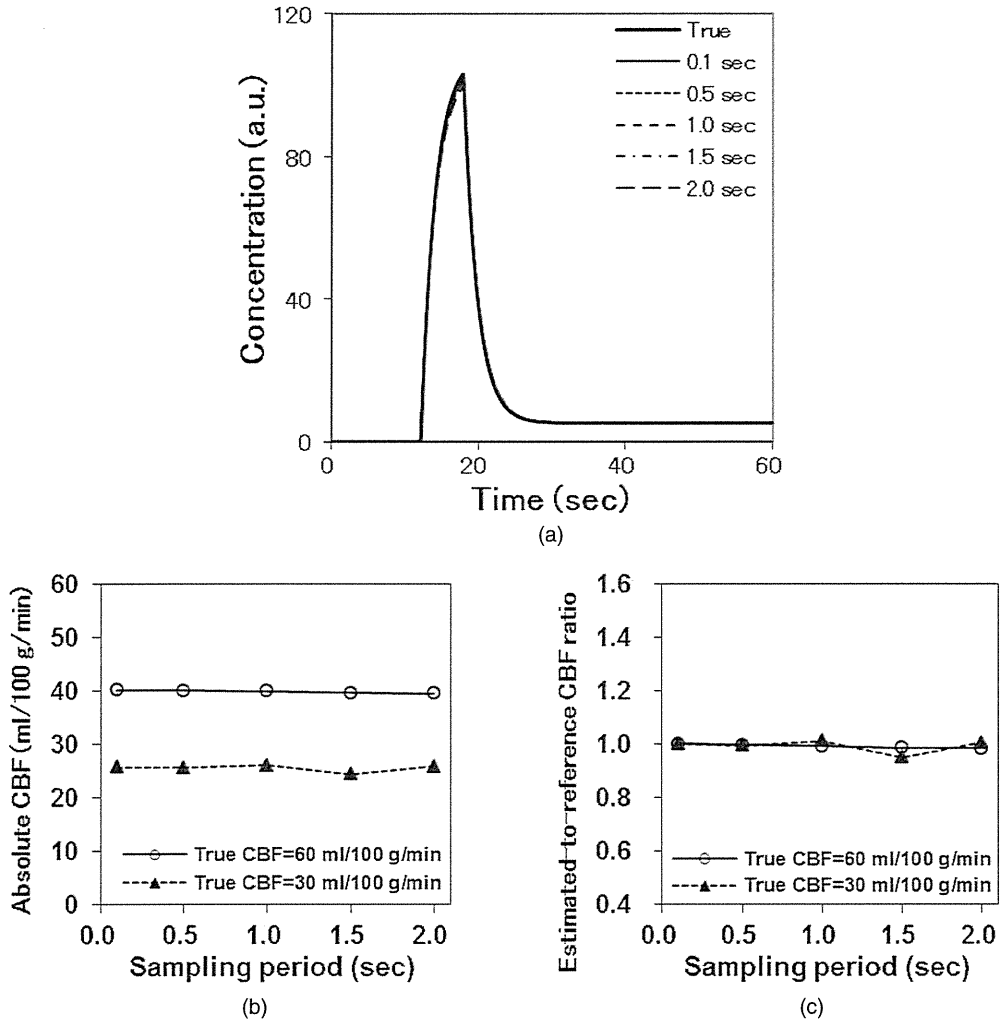

Figure 3. Effects of the sampling period on the shape of estimated arterial input functions (AIF) and calculated CBF values. For each sampling period, the AIF was reconstructed from 20 simulated tissue time–concentration curves according to the present method. (a) Variation of the shape of estimated AIFs due to sampling period. (b, c) Absolute CBF and relative CBF to a reference value at each sampling period are shown as a function of sampling period. Estimated-to-reference ratio is the ratio of the calculated CBF value at each sampling period to the reference CBF value obtained using the sampling period of 0.1 s.

the CBF values at the CBV value of 4.0 ml/100 g, even within the examined range of CBV, but was not dependent on the absolute CBF values (figures 4(b) and (c)).

Figure 5 shows the results of simulation study demonstrating the effects of regional differences of the tracer appearance time on the shape of the estimated AIFs and calculated CBF values. Increases in the difference in tracer arrival time caused dispersion of the reconstructed AIF (figure 5(a)) and increase in calculated CBF value (figures 5(b) and (c)). The increment reached 13% at Δt of 4 s, which simulated the situation in which the ROIs for reconstructing AIF are placed on a wide range from the top to the base of a cerebrum. Since actually ROIs

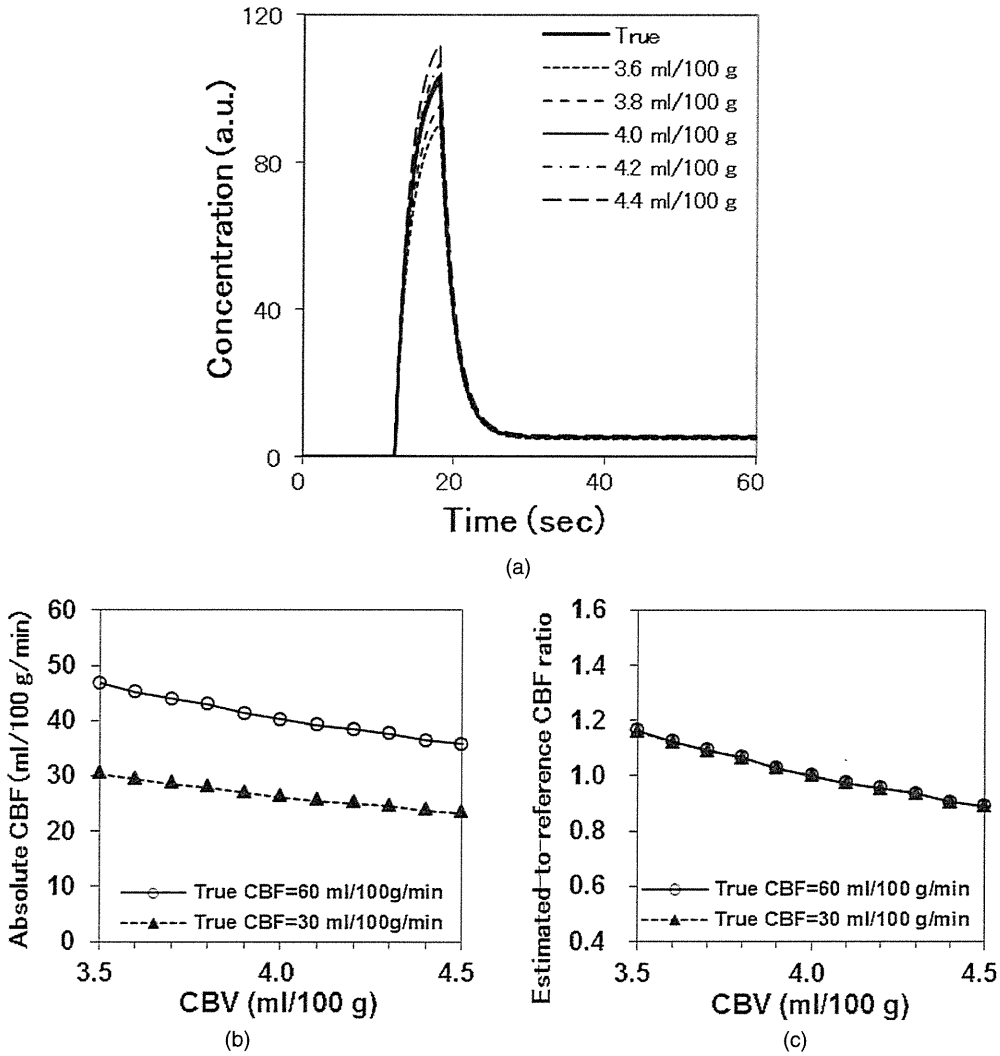

Figure 4. Effects of the deviation of the CBV value of the tissues, which are used for reconstructing arterial input function (AIF), from 4.0 ml/100 g on the shape of estimated AIFs and calculated CBF values. The AIFs were reconstructed from 20 simulated tissue time–concentration curves (TCC) according to the present method. The CBV value of the 20 tissue TCCs was varied in the range from 3.5 to 4.5 ml/100 g. (a) Variation of the shape of estimated AIFs due to the CBV value. (b, c) Absolute CBF and relative CBF to a reference value at each CBV value are shown as a function of the CBV value. Estimated-to-reference ratio is the ratio of the calculated CBF value at each CBV value to the reference CBF value obtained using the CBV value of 4.0 ml/100 g.

are placed within more restricted region of the cerebrum, the regional differences would have practically no influence on the estimated AIFs and calculated CBF values. Furthermore, the change in the calculated CBF due to the regional difference was not dependent on the absolute CBF values (figure 5(c)).

Figure 6 shows the results of the simulation study demonstrating the systematic error and COV in calculated CBF values, attributed to statistical noise in tissue TCCs. The mean CBF

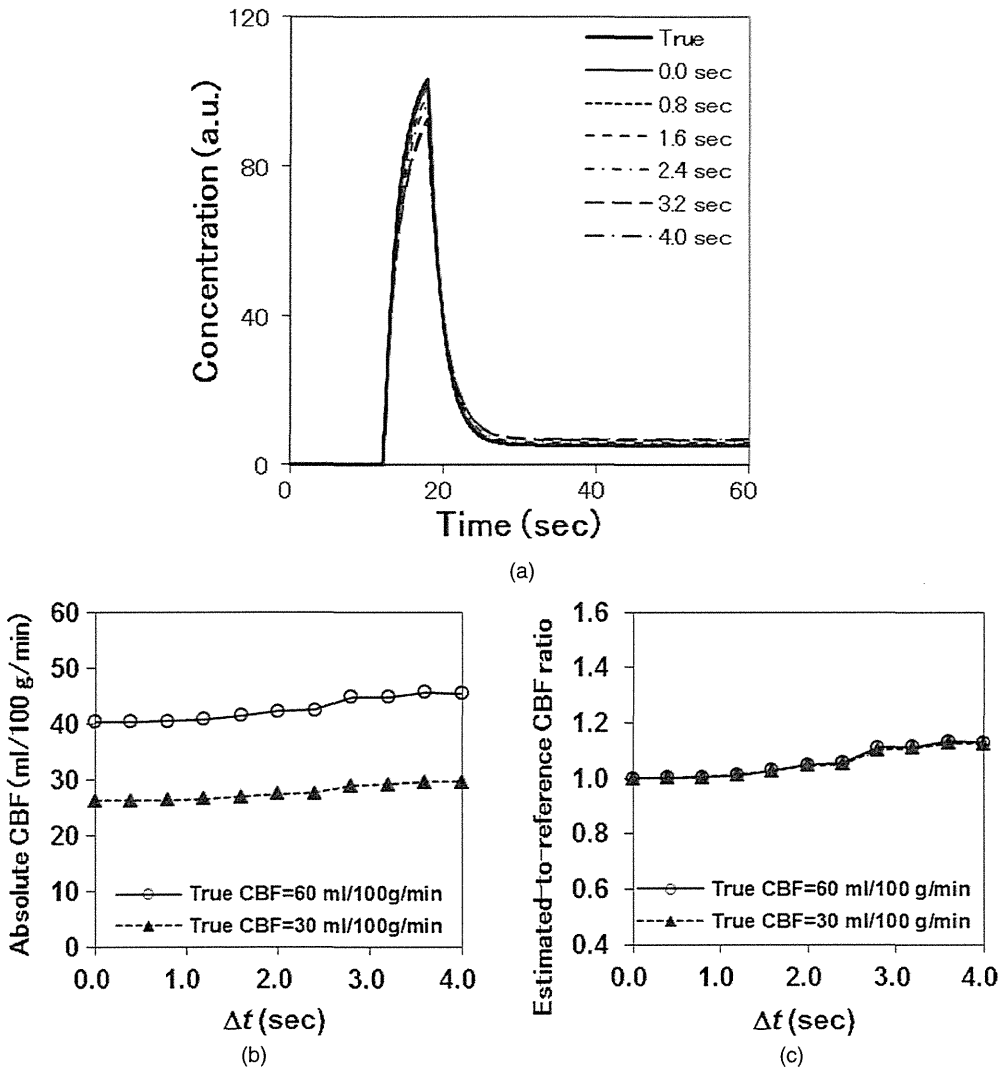

Figure 5. Effects of the regional difference of tracer appearance time among the tissues selected for reconstructing arterial input function (AIF) on the shape of estimated AIFs and calculated CBF values. The AIFs were reconstructed from 20 simulated tissue time–concentration curves (TCC) according to the present method. The Δt is the difference in tracer appearance time between earliest and latest TCCs out of the 20 TCCs. The Δt of 0.0 s means no difference in tracer appearance time among the TCCs. (a) Variation of the shape of estimated AIF due to Δt. (b, c) Absolute CBF and relative CBF to a reference value at each Δt value are shown as a function of Δt. Estimated-to-reference ratio is the ratio of the calculated CBF value at each Δt value to the reference CBF value obtained using the Δt of 0.0 s.

value increased with increasing noise level (figure 6(a)). The bias of the calculated CBF value reached 30% at noise COV of 8%, compared with the CBF value obtained from noise-free tissue TCCs (40.3 ml/100 g/min). The COV of the calculated CBF values also increased with increasing noise level, reaching 31% at noise COV of 8%. More than 2% noise COV resulted in a bias of more than 10% (figure 6(a)) and the COV of calculated CBF values more than 10% (figure 6(b)).

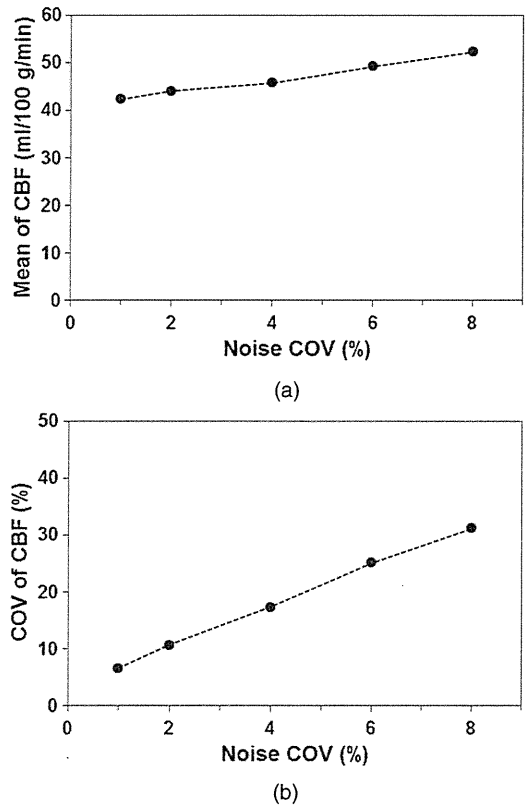

Figure 6. Effects of statistical noise on the CBF values calculated using the tissue-based method. (a) Relationship between the mean of calculated CBF values and noise COV. (b) Relationship between the COV of calculated CBF values and the noise COV. True CBF value was 60 ml/100 g/min.

3.2. Patient study

Figure 7 shows the TB-AIF and VS-AIF obtained from one patient. The height of TB-AIF was higher than that of VS-AIF (figure 7(a)). This tendency was observed in all patients. The ratio of heights between TB-AIF and VS-AIF was 4.2 $\pm$ 1.2. In figure 7(b), the heights of two AIFs were normalized to the same height in order to allow comparisons of their shapes. The shape of the first-pass period was similar between the two AIFs. On the other hand, the arterial voxel selection method overestimates at the tail part compared with the tissue-based method. This was seen in all patients.

Figure 8 shows TB-CBF, VS-CBF and PET-CBF images for a representative case, in which the subject had a left MCA occlusion. The PET-CBF images indicate lower CBF in the left hemisphere than the right hemisphere (L/R ratio of PET-CBF = 0.67). The contrast between left and right hemispheres in TB-CBF images was similar to those in VS-CBF, and was poorer in PET-CBF (L/R ratio of TB-CBF image = 0.69, L/R ratio of VS-CBF image = 0.69). The TB-CBF and VS-CBF images closely resembled each other. Similar results were obtained in all other cases.

Figure 9 shows the Bland–Altman plots for the measure of agreement between PET and either the tissue-based method or the arterial voxel selection method. The difference between

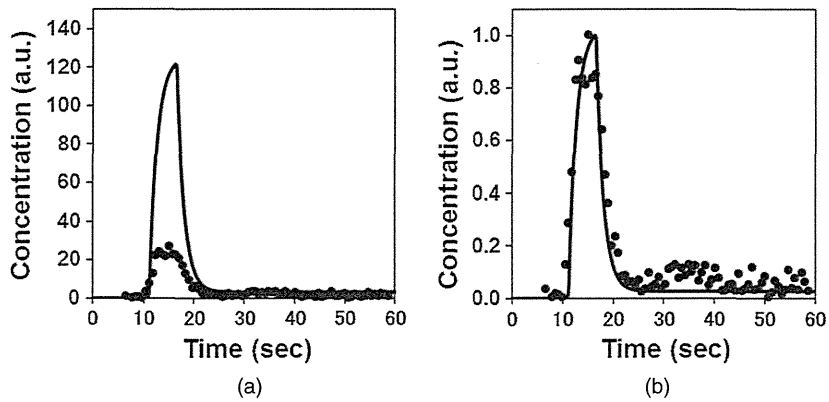

Figure 7. A typical example of the arterial input functions (AIF) obtained using the tissue-based method (solid line) and the arterial voxel selection method (black circle) obtained from a representative study. The height of the AIF obtained from the tissue-based method was approximately 4.5 times higher than that by the voxel selection method (a). After normalizing the two AIFs, the arterial voxel selection method overestimates at the tail part (b).

the tissue-based method and PET was -2.2 ± 7.4 ml/100 g/min ($r = 0.55$, $p < 0.01$) for quantitative CBF values and 0.07 ± 0.09 ($r = 0.82$, $p < 0.01$) for CBF ratios. The difference between the arterial voxel selection method and PET was -0.2 ± 8.2 ml/100 g/min ($r = 0.47$, $p = 0.01$) for quantitative CBF values and 0.07 ± 0.09 ($r = 0.83$, $p < 0.01$) for CBF ratios. The mean difference in CBF values was slightly larger for the tissue-based method than for the arterial voxel selection method, while the SD of the difference was slightly smaller for the tissue-based method than for the arterial voxel selection method. These results suggest that the CBF values obtained from the tissue-based and arterial voxel selection methods are comparable. Furthermore, the CBF ratios, indicating the contrast of CBF images, were also similar between the tissue-based method and the arterial voxel selection method.

4. Discussion

This study demonstrated that the AIF from tissue TCCs in DSC-MRI could be obtained using the tissue-based method by drawing multiple ROIs in the cerebral tissue regions, thus enabling quantitative assessment of CBF images in clinical settings without the need for careful drawing of an ROI on the cerebral artery regions. The AIFs obtained by the tissue-based method appeared to be essentially consistent as compared with TCCs directly obtained from the MCA regions, or the arterial voxel selection method (figure 7). CBF images obtained by the tissue-based method agreed with those by the arterial voxel selection method (figure 8). Reasonable agreement was seen in the quantitative CBF values as compared with those obtained by ^{15}O-water PET (figure 9). These results suggest the feasibility of the present tissue-based technique, being applicable to the quantitative assessment of CBF.

The technique avoids possible errors attributed to the partial volume effect, which likely causes underestimation of AIF around the peak, and overestimation at the tail. Note that the AIF observed using the arterial voxel selection method was smaller at peak than with the tissue-based method, as typically shown in figure 7(a). It should also be noted that AIFs were higher with the voxel-based method than those with the tissue-based method at the tail of AIF as shown in figure 7(b). The partial volume effect, namely the spill-out effects when

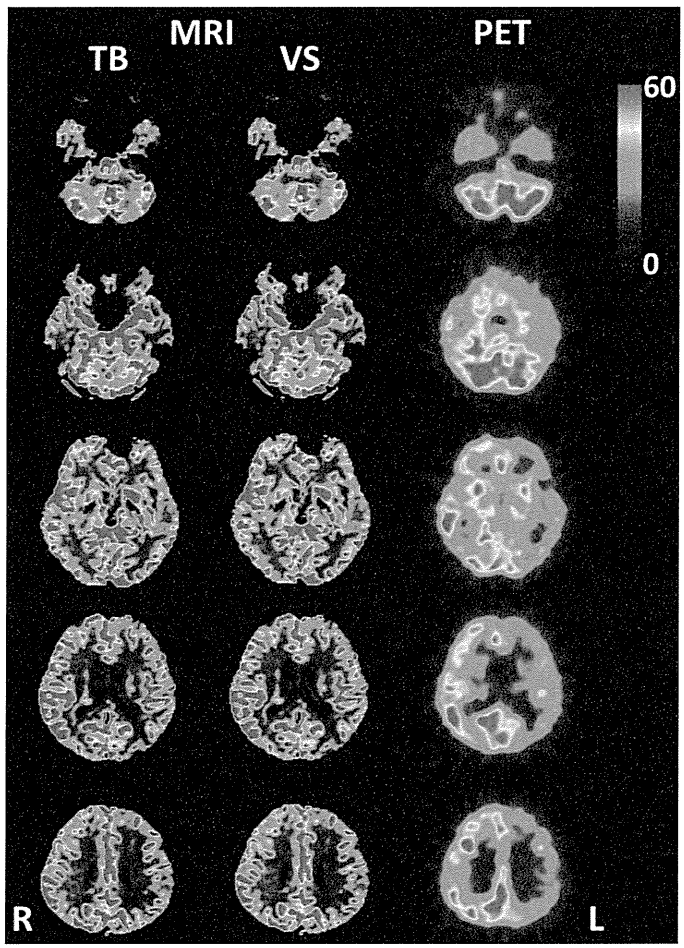

Figure 8. Comparison of cerebral blood flow (CBF) images obtained by the tissue-based method (TB), the arterial voxel selection method (VS), and positron emission tomography (PET) in a patient with left middle cerebral artery occlusion. Images were displayed using the same color scale with the maximum CBF of 60 ml/100 g/min.

the arterial TCC is higher than tissue TCC, and the spill-in effects when the arterial TCC is lower than tissue TCC, should be the reason for these observations, at least in a part. The reason for the good agreement of absolute CBF values between the arterial voxel selection and tissue-based methods, despite such discrepancies in AIFs, was because both methods involved a procedure for the absolute scaling. CBV was fixed at 4 ml/100 g in the gray matter region in the tissue-based method, while CBF was fixed at 22 ml/min/100g in the white matter in the arterial voxel selection method. These procedures empirically provided the absolute scale of AIFs being consistent between the two methods.

The tissue-based method is also advantageous in terms of increasing the dynamic range of MR signals in tissue or increased signal-to-noise ratio in tissue regions, due to the avoidance of the need for the direct assessment of AIF from the artery region. It should be noted that the nonlinear relationship between the tracer concentration and the relaxation rate has been a source of errors, particularly in the determination of AIF from the arterial TCC, which has higher contrasts than in the cerebral tissue. Although a model has been proposed to correct

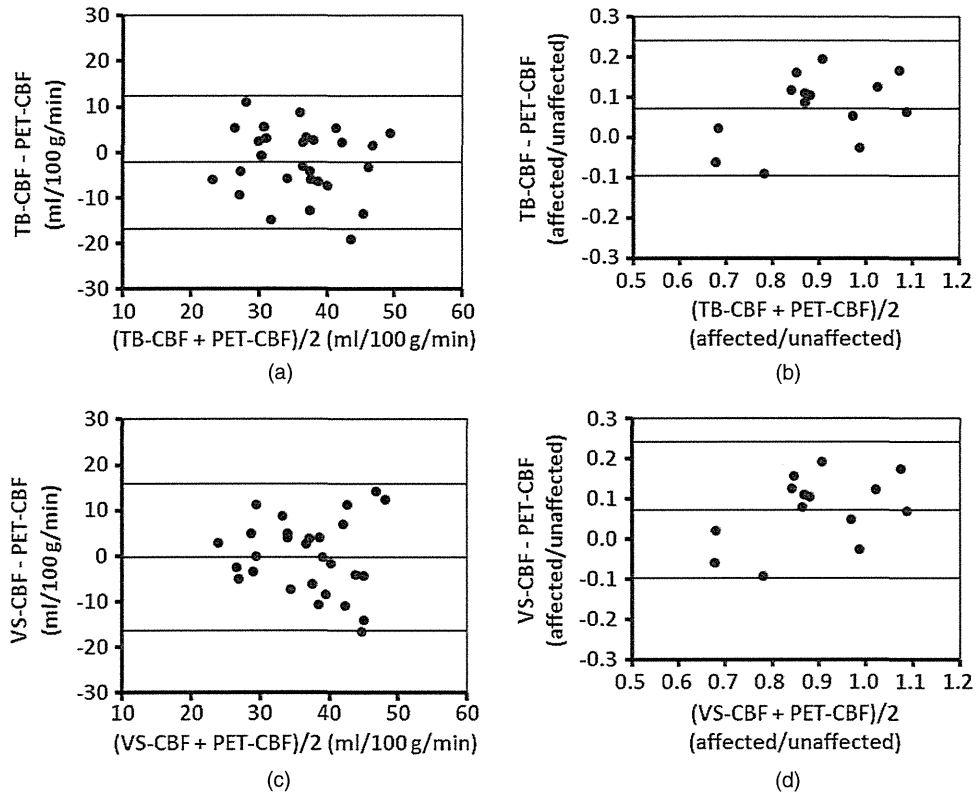

Figure 9. Bland–Altman plots which compares CBF values between DSC-MRI and PET. (a) Absolute CBF values from the tissue-based method versus PET; (b) CBF ratios between affected and unaffected hemispheres from the tissue-based method versus PET; (c) absolute CBF values from the arterial voxel selection method versus PET; (d) CBF ratios between affected and unaffected hemispheres from the arterial voxel selection method versus PET. Middle lines represent mean difference; upper and lower lines represent mean ± 1.96 SD.

for the nonlinear signal intensity in the carotid artery region, providing the true TCC with reasonable accuracy (van Osch *et al* 2003), a special pulse sequence is required in order to guarantee the dynamic range of MR signals in both tissue and artery. The tissue-based method should contribute to the increase of the dynamic range of MR signals, or the increased signal-to-noise ratio in tissue regions, without a special imaging technique. The quantitative accuracy of CBF assessment may therefore be improved in practical situations, but a further study is warranted to confirm this.

The tissue-based method enables us to eliminate stringent constraints in slice selection procedures. The number of slice acquisition has been limited in DSC-MRI, largely attributed to the need for high temporal resolution required for tracking AIFs after bolus administration of contrast agents. The number of imaging slices was 10–15 slices in EPI acquisitions with typical TR values using conventional MR scanners (Calamante *et al* 1999), thus limiting the imaging slices only a part of the whole brain. Selection of an optimal slice is also suggested in order to achieve the accurate determination of AIF (Kikuchi *et al* 2001, van Osch *et al* 2002). The constraints of containing major cerebral arteries in the imaging slices and the slice angles for accurate determination of AIF can be a restriction in some clinical studies. Although the

number of imaging slices can be increased by the introduction of parallel imaging techniques (Ulmer *et al* 2010, Server *et al* 2011), the tissue-based method is still attractive due to its flexibility in defining the imaging slices, benefiting studies of DSC-MRI.

The present tissue-based method is essentially the same as the one proposed by Schabel *et al* (2010a) and (2010b) for assessing the permeability of Gadolinium-contrast agent. The present report is the first one that demonstrated the applicability for quantitative assessment of CBF using the DSC-MRI technique. An essential finding was that the method can provide AIFs using smaller number of model parameters to describe the shape of AIF. Our formulation for AIF consists of 4 parameters, while Schabel's model consists of 11 parameters. The model formulation comprising a smaller number of parameters enables faster and reliable estimates of AIFs and thus quantitative CBF images. It should be noted that this simplified formulation enabled stable estimation of hepatic blood flow using $H_2{}^{15}O$ PET (Kudomi *et al* 2008) and hepatic fluorodeoxyglucose accumulation using ^{18}F-FDG and PET (Kudomi *et al* 2009). There might be several other applications to CT-perfusion and quantitative SPECT studies.

The first set of simulations shown in figure 2 demonstrated that systematic errors could be introduced in calculated CBF values if AIF is not properly determined. In particular, estimated CBF values are sensitive to A, the parameter that describes to the height of the bolus peak. However, the magnitude of errors is less sensitive to other parameters that represent the height of the tail and/or the width of the bolus. It was also shown that the magnitude of errors had almost no flow dependence, suggesting minimal effects to the high-to-low contrast in CBF images. The simulations shown in figures 3 and 5 demonstrated that almost no errors could be introduced attributed to the prolonged sampling period nor regional difference of the tracer appearance time. However, absolute CBF estimates are highly dependent on the CBV values which have to be assumed for reconstructing the AIF from the observed multiple tissue TCCs (figure 4). This is essentially attributed to the CBF values largely affected by the A value that described the height of AIF shown in figure 2. It is worthy of note, however, that the calculated-to-reference ratio of the CBF showed the same tendency, suggesting the high-to-low ratio of the calculated CBF values not being dependent on any source of errors.

Another set of simulation study demonstrated that statistical noise in the tissue TCCs could not only cause notable statistical uncertainty but also the systematic errors in the calculated CBF values. However, the changes in the calculated CBF were shown to be only small. Typical noise level in tissue TTCs is approximately 6% COV for a single pixel at a single frame of DSC-MRI images in the present study. This causes a systematic bias in CBF by approximately 22%. Since 3 $\times$ 3 pixel smoothing has been applied in this work, as has been suggested in several previous works (Østergaard *et al* 1996a, Ibaraki *et al* 2005), approximately 2% COV causes only 9% bias in the calculated CBF values. The image smoothing which is a standard procedure (Østergaard *et al* 1996a, Ibaraki *et al* 2005) causes systematic errors in the arterial voxel selection method due to the increased partial volume effect. However, this is not the case in the tissue-based method, which is another advantage of the tissue-based method.

Direct comparison of CBF images between DSC-MRI and ^{15}O-water PET demonstrated lower contrast in the former compared with the latter. This is attributed to an essential limitation of the SVD technique. Previous simulation studies have shown that SVD underestimates the CBF when MTT is short, attributed to the limited accuracy of tissue impulse response (Wu *et al* 2003b, Carpenter *et al* 2006). Several other techniques have been proposed based on improved deconvolution procedures (Vonken *et al* 1999, Calamante *et al* 2003, Chen *et al* 2005, Willats *et al* 2006). Such techniques for improved deconvolution may further improve the accuracy of the present tissue-based method.

The limitation of the present method is the need for assuming the CBV value of the tissues selected for reconstructing AIF as 4.0 ml/100 g. As demonstrated by the simulation study,

this is the most critical source of errors. Further study should be carried out to investigate the magnitude of errors in realistic diseased conditions. This requires larger scale of clinical studies. An additional potential source of errors in the tissue-based method might arise from a limitation of the model formulation for tissue impulse response, assumed as a single-compartment model or a single-exponential function in this study. Although more realistic models may exist, the single-exponential function has most often been employed in previous work. Reasonable results have been obtained in this study. Further study may however be desired in order to improve the accuracy of the tissue-based approach.

5. Conclusion

AIF could be well reconstructed from multiple tissue TCCS in DSC-MRI, enabling quantitative assessment of CBF images. Significant errors could be caused by errors in the assumed CBV values, but the relative contrast was shown to be rather stable. Although further careful evaluation is needed, the present tissue-based method avoids the naïve determination of AIFs defining ROIs on the cerebral artery regions. Enhanced dynamic range may further improve the accuracy of quantitative CBF assessment in DSC-MRI.

Acknowledgments

The authors declare no conflict of interest. We thank Dr Hiroshi Watabe for helpful support and Dr Ikuhiro Kida for helpful discussions. This study was partly supported by a grant from the New Energy and Industrial Technology Development Organization (NEDO) of Japan, and partly by a research grant on Advanced Medical Technology from the Ministry of Health, Labour and Welfare (MHLW) of Japan.

Appendix

A model function for AIF was created, by assuming a two-compartment model, in which the tracer is administered in a rectangular form and diffuses bi-directionally between arterial and interstitial space in whole body peripheral tissue compartments. Differential equations for the model function ($C_{\mathrm{Artery}}(t)$) can be expressed as

$$\frac{\mathrm{d}C_{\mathrm{Artery}}(t)}{\mathrm{d}t} = \frac{\mathrm{d}F}{\mathrm{d}t} - K_e C_{\mathrm{Artery}}(t) + K_i C_{\mathrm{WB}}(t) \tag{A.1}$$

$$\frac{\mathrm{d}C_{\mathrm{WB}}(t)}{\mathrm{d}t} = K_e C_{\mathrm{Artery}}(t) - K_i C_{\mathrm{WB}}(t) \tag{A.2}$$

$$\frac{\mathrm{d}F}{\mathrm{d}t} = \begin{array}{ll} A & (t_1 \leqslant t \leqslant t_2) \\ 0 & (\text{elsewhere}) \end{array} \tag{A.3}$$

where t_1 and t_2 assume the appearance time of administered tracer and $t_2 - t_1$ represents the administration duration, A corresponds to the given amount of tracer. Equation F (equation (A.3)) represents the bolus administration of tracer in the rectangular form with duration $t_2 - t_1$. $C_{\mathrm{WB}}(t)$ is the expected tracer concentration in interstitial spaces in whole body peripheral tissues, K_e and K_i are bidirectional tracer diffusion rates between blood and peripheral tissue compartments, respectively. Solving equation (A.2) for C_{WB} gives

$$C_{\mathrm{WB}}(t) = K_e \mathrm{e}^{-Ki \cdot t} \int_0^t C_{\mathrm{Artery}}(\tau) \mathrm{e}^{Ki \cdot \tau} \mathrm{d}\tau. \tag{A.4}$$

Sum of equations (A.1) and (A.2) is

$$\frac{d(C_{Artery}(t)+C_{WB}(t))}{dt}=\frac{dF}{dt}. \tag{A.5}$$

Thus,

$$\begin{aligned} C_{Artery}(t)+C_{WB}(t) &= F \\ &= 0 && (t<t_1) \\ &= A(t-t_1) && (t_1\leqslant t\leqslant t_2) \\ &= A(t_2-t_1) && (t>t_2). \end{aligned} \tag{A.6}$$

Substitution of C_{WB} from equations (A.4) into (A.6) after multiplying $e^{Ki\cdot t}$, gives

$$e^{Ki\cdot t}C_{Artery}(t)+K_e\int_0^t C_{Artery}(\tau)\,e^{Ki\cdot\tau}d\tau=e^{Ki\cdot t}F. \tag{A.7}$$

Differentiation with respect to t after arranging gives

$$\frac{dC_{Artery}(t)}{dt}=\alpha F+\frac{1}{K_e}\frac{dF}{dt}-K_e(1+\alpha)C_{Aetery}(t), \tag{A.8}$$

where $\alpha=K_i/K_e$. Thus,

$$C_{Artery}(t)=K_e e^{-Ke\cdot(1+\alpha)\cdot t}\int_0^t\left(\alpha F+\frac{1}{K_e}\frac{dF}{dt}\right)e^{Ke\cdot(1+\alpha)\cdot\tau}d\tau. \tag{A.9}$$

Solving equation (A.9), we obtain

$$\begin{aligned} C_{Artery}(t) &= 0 && (t<t_1) \\ &= \frac{A}{K_e^2(1+\alpha)^2}(K_e\alpha(1+\alpha)(t-t_1)+1-e^{Ke\cdot(1+\alpha)\cdot(t_1-t)}) && (t_1\leqslant t\leqslant t_2) \\ &= \frac{A}{K_e^2(1+\alpha)^2}(K_e\alpha(1+\alpha)(t_2-t_1)+e^{Ke\cdot(1+\alpha)\cdot(t_2-t)} \\ &\quad -e^{Ke\cdot(1+\alpha)\cdot(t_1-t)}) && (t>t_2). \end{aligned} \tag{A.10}$$

The first term in the second equation for $t_1<t<t_2$, i.e. $K_e\alpha(1+\alpha)(t-t_1)$ would complicate further calculations, thus this term was omitted, and the model function (A.10) was modified to set the C_{Artery} value as 0 at $t=t_1$, as continuous at $t=t_2$, and as non-zero value at the equilibrium, i.e. at $t=\infty$. Thus, following equation was derived:

$$\begin{aligned} C_{Artery}(t) &= 0. && (t<t_1) \\ &= \frac{A}{K_e^2(1+\alpha)^2}[1-\exp\{K_e(1+\alpha)(t_1-t)\}] && (t_1\leqslant t\leqslant t_2) \\ &= \frac{A}{K_e^2(1+\alpha)^2}[\exp\{K_e(1+\alpha)(t_1-t_2)\}+\exp\{K_e(1+\alpha)(t_2-t)\} \\ &\quad -2\cdot\exp\{K_e(1+\alpha)(t_1-t)\}] && (t>t_2). \end{aligned} \tag{A.11}$$

References

Bland J M and Altman D G 1986 Statistical methods for assessing agreement between two methods of clinical measurement *Lancet* **1** 307–10

Bland J M and Altman D G 1999 Measuring agreement in method comparison studies *Stat. Methods Med. Res.* **8** 135–60

Brix G, Kiessling F, Lucht R, Darai S, Wasser K, Delorme S and Griebel J 2004 Microcirculation and microvasculature in breast tumors: pharmacokinetic analysis of dynamic MR image series *Magn. Reson. Med.* **52** 420–9

Calamante F, Gadian D G and Connelly A 2000 Delay and dispersion effects in dynamic susceptibility contrast MRI: simulations using singular value decomposition *Magn. Reson. Med.* **44** 466–73

Calamante F, Gadian D G and Connelly A 2003 Quantification of bolus-tracking MRI: improved characterization of the tissue residue function using Tikhonov regularization *Magn. Reson. Med.* **50** 1237–47

Calamante F, Thomas D L, Pell G S, Wiersma J and Turner R 1999 Measuring cerebral blood flow using magnetic resonance imaging techniques *J. Cereb. Blood Flow Metab.* **19** 701–35

Calamante F, Vonken E J and van Osch M J 2007 Contrast agent concentration measurements affecting quantification of bolus-tracking perfusion MRI *Magn. Reson. Med.* **58** 544–53

Carpenter T K, Armitage P A, Bastin M E and Wardlaw J M 2006 DSC perfusion MRI-quantification and reduction of systematic errors arising in areas of reduced cerebral blood flow *Magn. Reson. Med.* **55** 1342–9

Carroll T J *et al* 2002 Absolute quantification of cerebral blood flow with magnetic resonance, reproducibility of the method, and comparison with $H_2(15)O$ positron emission tomography *J. Cereb. Blood Flow Metab.* **22** 1149–56

Chen J J, Smith M R and Frayne R 2005 Advantages of frequency-domain modeling in dynamic-susceptibility contrast magnetic resonance cerebral blood flow quantification *Magn. Reson. Med.* **53** 700–7

Fritz-Hansen T, Rostrup E, Larsson H B, Sondergaard L, Ring P and Henriksen O 1996 Measurement of the arterial concentration of Gd-DTPA using MRI: a step toward quantitative perfusion imaging *Magn. Reson. Med.* **36** 225–31

Hansen A E, Pedersen H, Rostrup E and Larsson H B 2009 Partial volume effect (PVE) on the arterial input function (AIF) in T1-weighted perfusion imaging and limitations of the multiplicative rescaling approach *Magn. Reson. Med.* **62** 1055–9

Hatazawa J *et al* 1995 Regional cerebral blood flow, blood volume, oxygen extraction fraction, and oxygen utilization rate in normal volunteers measured by the autoradiographic technique and the single breath inhalation method *Ann. Nucl. Med.* **9** 15–21

Henkelman R M 1985 Measurement of signal intensities in the presence of noise in MR images *Med. Phys.* **12** 232–3

Hirano T, Minematsu K, Hasegawa Y, Tanaka Y, Hayashida K and Yamaguchi T 1994 Acetazolamide reactivity on ^{123}I-IMP single photon emission computed tomography in patients with major cerebral artery occlusive disease: correlation with positron emission tomography parameters *J. Cereb. Blood Flow Metab.* **14** 763–70

Ibaraki M, Shimosegawa E, Toyoshima H, Takahashi K, Miura S and Kanno I 2005 Tracer delay correction of cerebral blood flow with dynamic susceptibility contrast-enhanced MRI *J. Cereb. Blood Flow Metab.* **25** 378–90

Iida H, Miura S, Kanno I, Murakami M, Takahashi K and Uemura K 1989 Design and evaluation of headtome-IV, a whole-body positron emission tomograph *IEEE Trans. Nucl. Sci.* **37** 1006–110

Iida H, Miura S, Shoji Y, Ogawa T, Kado H, Narita Y, Hatazawa J, Eberl S, Kanno I and Uemura K 1998 Noninvasive quantitation of cerebral blood flow using oxygen-15-water and a dual-PET system *J. Nucl. Med.* **39** 1789–98

Ito H, Yokoyama I, Iida H, Kinoshita T, Hatazawa J, Shimosegawa E, Okudera T and Kanno I 2000 Regional differences in cerebral vascular response to $PaCO_2$ changes in humans measured by positron emission tomography *J. Cereb. Blood Flow Metab.* **20** 1264–70

Ito H, Yokoyama I, Tamura Y, Kinoshita T, Hatazawa J, Kawashima R and Iida H 2002 Regional changes in human cerebral blood flow during dipyridamole stress: neural activation in the thalamus and prefrontal cortex *Neuroimage* **16** 788–93

Ito H *et al* 2004 Database of normal human cerebral blood flow, cerebral blood volume, cerebral oxygen extraction fraction and cerebral metabolic rate of oxygen measured by positron emission tomography with ^{15}O-labelled carbon dioxide or water, carbon monoxide and oxygen: a multicentre study in Japan *Eur. J. Nucl. Med. Mol. Imaging* **31** 635–43

Kikuchi K, Murase K, Miki H, Kikuchi T, Sugawara Y, Mochizuki T, Ikezoe J and Ohue S 2001 Measurement of cerebral hemodynamics with perfusion-weighted MR imaging: comparison with pre- and post-acetazolamide 133Xe-SPECT in occlusive carotid disease *AJNR Am. J. Neuroradiol.* **22** 248–54

Kudomi N, Choi E, Watabe H, Kim K, Shidahara M, Ogawa M, Teramoto N, Sakamoto E and Iida H 2003 Development of a GSO detector assembly for a continuous blood sampling system *IEEE Trans. Nucl. Sci.* **50** 70–3

Kudomi N *et al* 2008 Non-invasive estimation of hepatic blood perfusion from H(2) (15)O PET images using tissue-derived arterial and portal input functions *Eur. J. Nucl. Med. Mol. Imaging* **35** 1899–911

Kudomi N *et al* 2009 Non-invasive estimation of hepatic glucose uptake from [18F]FDG PET images using tissue-derived input functions *Eur. J. Nucl. Med. Mol. Imaging* **36** 2014–26

Larsson H B, Stubgaard M, Frederiksen J L, Jensen M, Henriksen O and Paulson O B 1990 Quantitation of blood-brain barrier defect by magnetic resonance imaging and gadolinium-DTPA in patients with multiple sclerosis and brain tumors *Magn. Reson. Med.* **16** 117–31

Østergaard L, Sorensen A G, Kwong K K, Weisskoff R M, Gyldensted C and Rosen B R 1996a High resolution measurement of cerebral blood flow using intravascular tracer bolus passages. Part II: experimental comparison and preliminary results *Magn. Reson. Med.* **36** 726–36

Østergaard L, Weisskoff R M, Chesler D A, Gyldensted C and Rosen B R 1996b High resolution measurement of cerebral blood flow using intravascular tracer bolus passages. Part I: mathematical approach and statistical analysis *Magn. Reson. Med.* **36** 715–25

Rosen B R, Belliveau J W, Vevea J M and Brady T J 1990 Perfusion imaging with NMR contrast agents *Magn. Reson. Med.* **14** 249–65

Salluzzi M, Frayne R and Smith M R 2005 An alternative viewpoint of the similarities and differences of SVD and FT deconvolution algorithms used for quantitative MR perfusion studies *Magn. Reson. Imaging* **23** 481–92

Schabel M C, DiBella E V, Jensen R L and Salzman K L 2010a A model-constrained Monte Carlo method for blind arterial input function estimation in dynamic contrast-enhanced MRI: II. *In vivo* results *Phys. Med. Biol.* **55** 4807–23

Schabel M C, Fluckiger J U and DiBella E V 2010b A model-constrained Monte Carlo method for blind arterial input function estimation in dynamic contrast-enhanced MRI: I. Simulations *Phys. Med. Biol.* **55** 4783–806

Server A, Orheim T E, Graff B A, Josefsen R, Kumar T and Nakstad P H 2011 Diagnostic examination performance by using microvascular leakage, cerebral blood volume, and blood flow derived from 3-T dynamic susceptibility-weighted contrast-enhanced perfusion MR imaging in the differentiation of glioblastoma multiforme and brain metastasis *Neuroradiology* **53** 319–30

Shidahara M *et al* 2002 Evaluation of a commercial PET tomograph-based system for the quantitative assessment of rCBF, rOEF and $rCMRO_2$ by using sequential administration of ^{15}O-labeled compounds *Ann. Nucl. Med.* **16** 317–27

Smith A M, Grandin C B, Duprez T, Mataigne F and Cosnard G 2000 Whole brain quantitative CBF and CBV measurements using MRI bolus tracking: comparison of methodologies *Magn. Reson. Med.* **43** 559–64

Smith M R, Lu H, Trochet S and Frayne R 2004 Removing the effect of SVD algorithmic artifacts present in quantitative MR perfusion studies *Magn. Reson. Med.* **51** 631–4

Ulmer S, Hartwigsen G, Riedel C, Jansen O, Mehdorn H M and Nabavi A 2010 Intraoperative dynamic susceptibility contrast MRI (iDSC-MRI) is as reliable as preoperatively acquired perfusion mapping *Neuroimage* **49** 2158–62

van Osch M J, Rutgers D R, Vonken E P, van Huffelen A C, Klijn C J, Bakker C J and van der Grond J 2002 Quantitative cerebral perfusion MRI and CO_2 reactivity measurements in patients with symptomatic internal carotid artery occlusion *Neuroimage* **17** 469–78

van Osch M J, Vonken E J, Bakker C J and Viergever M A 2001 Correcting partial volume artifacts of the arterial input function in quantitative cerebral perfusion MRI *Magn. Reson. Med.* **45** 477–85

van Osch M J, Vonken E J, Viergever M A, van der Grond J and Bakker C J 2003 Measuring the arterial input function with gradient echo sequences *Magn. Reson. Med.* **49** 1067–76

Vonken E P, Beekman F J, Bakker C J and Viergever M A 1999 Maximum likelihood estimation of cerebral blood flow in dynamic susceptibility contrast MRI *Magn. Reson. Med.* **41** 343–50

Willats L, Connelly A and Calamante F 2006 Improved deconvolution of perfusion MRI data in the presence of bolus delay and dispersion *Magn. Reson. Med.* **56** 146–56

Wu O, Østergaard L, Koroshetz W J, Schwamm L H, O'Donnell J, Schaefer P W, Rosen B R, Weisskoff R M and Sorensen A G 2003a Effects of tracer arrival time on flow estimates in MR perfusion-weighted imaging *Magn. Reson. Med.* **50** 856–64

Wu O, Østergaard L, Weisskoff R M, Benner T, Rosen B R and Sorensen A G 2003b Tracer arrival timing-insensitive technique for estimating flow in MR perfusion-weighted imaging using singular value decomposition with a block-circulant deconvolution matrix *Magn. Reson. Med.* **50** 164–74

Yamaguchi T, Kanno I, Uemura K, Shishido F, Inugami A, Ogawa T, Murakami M and Suzuki K 1986 Reduction in regional cerebral metabolic rate of oxygen during human aging *Stroke* **17** 1220–8

Yang C, Karczmar G S, Medved M and Stadler W M 2004 Estimating the arterial input function using two reference tissues in dynamic contrast-enhanced MRI studies: fundamental concepts and simulations *Magn. Reson. Med.* **52** 1110–7

Yang C, Karczmar G S, Medved M and Stadler W M 2007 Multiple reference tissue method for contrast agent arterial input function estimation *Magn. Reson. Med.* **58** 1266–75

Journal of Cerebral Blood Flow & Metabolism (2012) 32, 2066–2075

www.jcbfm.com

Cerebral blood flow and metabolism of hyperperfusion after cerebral revascularization in patients with moyamoya disease

Yasuyuki Kaku[1], Koji Iihara[1], Norio Nakajima[1], Hiroharu Kataoka[1], Kenji Fukuda[1], Jun Masuoka[1], Kazuhito Fukushima[2], Hidehiro Iida[3] and Nobuo Hashimoto[1]

[1]*Department of Neurosurgery, National Cerebral and Cardiovascular Center, Osaka, Japan;* [2]*Department of Radiology, National Cerebral and Cardiovascular Center, Osaka, Japan;* [3]*Department of Investigative Radiology, National Cerebral and Cardiovascular Center Research Institute, Osaka, Japan*

In moyamoya disease (MMD), surgical revascularization may be complicated with postoperative hyperperfusion. We analyzed cerebral perfusion and metabolism using positron emission tomography (PET) or single-photon emission computed tomography (SPECT) before and after bypass surgery on 42 sides of 34 adult patients with MMD. In seven cases (16.7%) with symptomatic hyperperfusion, diagnosed by qualitative ^{123}I-iodoamphetamine (IMP) SPECT, a subsequent PET study during postoperative subacute stages revealed significantly increased cerebral blood flow (CBF) from 34.1 ± 8.2 to 74.3 ± 12.8 mL/100 g per minute ($P<0.01$), a persistent increase in cerebral blood volume (CBV) from 5.77 ± 1.67 to 7.01 ± 1.44 mL/100 g and a significant decrease in oxygen extraction fraction (OEF) from 0.61 ± 0.09 to 0.40 ± 0.08 ($P<0.01$). Mean absolute CBF values during symptomatic hyperperfusion were more than the normal control +2 standard deviations, the predefined criteria of PET. Interestingly, two patients with markedly increased cerebral metabolic rate of oxygen ($CMRO_2$) at hyperperfusion were complicated with postoperative seizure. Among preoperative PET parameters, increased OEF was the only significant risk factor for symptomatic hyperperfusion ($P<0.05$). This study revealed that symptomatic hyperperfusion in MMD is characterized by temporary increases in CBF >100% over preoperative values caused by prolonged recovery of increased CBV.
Journal of Cerebral Blood Flow & Metabolism (2012) **32,** 2066–2075; doi:10.1038/jcbfm.2012.110; published online 1 August 2012

Keywords: hyperperfusion; moyamoya disease; positron emission tomography

Introduction

The causes of moyamoya disease (MMD), characterized by progressive stenosis/occlusion of the terminal internal cerebral artery and its branches, are unclear; ischemic and hemorrhage injuries may be the causes of MMD (Suzuki and Takaku, 1969). Superficial temporal artery (STA)-middle cerebral artery (MCA) anastomosis or various kinds of indirect bypasses are recommended for symptomatic patients based on the degree of hemodynamic compromise (Kuroda and Houkin, 2008; Takahashi and Miyamoto, 2010). Despite favorable long-term outcomes after successful bypass surgery for MMD, increasing evidence suggests that this may be complicated with temporary neurologic deterioration during the postoperative acute stage owing to focal cerebral hyperperfusion around the site of the anastomosis (Fujimura *et al*, 2007, 2009, 2011; Furuya *et al*, 2004; Kim *et al*, 2008; Ogasawara *et al*, 2005). Postoperative cerebral hyperperfusion is defined as a major increase in ipsilateral cerebral blood flow (CBF) well above the metabolic demands of brain tissue (Piepgras *et al*, 1988; Sundt *et al*, 1981), and is well characterized in patients after carotid endarterectomy (CEA). Although a similar cerebral hyperperfusion phenomenon was reported in patients with MMD using single-photon emission computed tomography (SPECT) or xenon-enhanced computed tomography (Fujimura *et al*, 2007, 2009, 2011; Furuya *et al*, 2004; Kim *et al*, 2008; Ogasawara *et al*, 2005), no previous study has quantitatively analyzed CBF and metabolism of postoperative hyperperfusion in MMD. The purpose of this study was to analyze CBF and metabolism by positron emission tomography (PET) in cases of symptomatic cerebral hyperperfusion, screened by qualitative

Correspondence: Dr K Iihara, Department of Neurosurgery, National Cerebral and Cardiovascular Center, 5-7-1 Fujishiro-dai Suita, Osaka 565-8565, Japan.
E-mail: kiihara@hsp.ncvc.go.jp
This work was supported by Health Labour Sciences Research Grant from the Ministry of Health, Labour and Welfare of Japan.
Received 10 February 2012; revised 22 May 2012; accepted 4 July 2012; published online 1 August 2012

^{123}I-iodoamphetamine (^{123}I-IMP) SPECT as previously reported, after STA-MCA anastomosis in patients with MMD. Relative increases and absolute values of CBF in PET during symptomatic hyperperfusion in MMD were compared with those of the traditional definition of post CEA hyperperfusion and the predefined CBF value as normal control + 2 standard deviations (s.d.).

Materials and methods

Patient Population

This study protocol was governed by the guidelines of national government based on the Helsinki Declaration revised in 1983, and it was approved by the Institutional Research and Ethics Committee of our hospital. All study participants provided informed consent in the study. Between April 2009 and June 2011, 34 patients (21 women) with MMD were treated at the Department of Neurosurgery, National Cerebral and Cardiovascular Center, Osaka, Japan; age (mean ± s.d.) was 39.3 ± 15.3 years (range, 15 to 70 years). Pediatric patients were excluded from the study. Diagnosis of MMD was based on cerebral angiography studies according to diagnostic criteria updated in 1997 (Fukui, 1997). Presenting symptoms were cerebral infarction ($n = 13$), transient ischemic attack ($n = 24$), involuntary movements ($n = 2$), and intracerebral/intraventricular hemorrhage ($n = 3$). The STA-MCA bypass surgery was performed on 42 hemispheres of these patients.

Surgical Procedure

All patients were treated by the same surgeons (KI and NN). Under general anesthesia mainly using propofol, the parietal and/or frontal branches of the STA were dissected, and single and/or double anastomosis to supra- and/or infra-Sylvian MCA (M4) was performed in a side-to-end manner. The patency of the anastomoses was intraoperatively confirmed by Doppler ultrasonography and indocyanine green videoangiography.

Diagnosis of Symptomatic and Asymptomatic Hyperperfusion Based on Perioperative Positron Emission Tomography and Single-Photon Emission Computed Tomography Studies

The protocol of the perioperative measurement of CBF with/without metabolism was shown in Figure 1. The PET or *N*-isopropyl-*p*-[^{123}I] IMP SPECT was conducted preoperatively (within 1 month of the operation). Preoperative PET was performed mainly for patients with severe ischemic symptoms. As for screening, ^{123}I-IMP SPECT was conducted first during postoperative day (POD) 1 to 3 for all patients to determine qualitatively the presence of a significant focal increase in CBF at the site of anastomosis. Patients associated with other pathologies such as mass effect by the swollen temporal muscle used for indirect anastomosis, subdural/epidural hematoma, and postoperative new frank

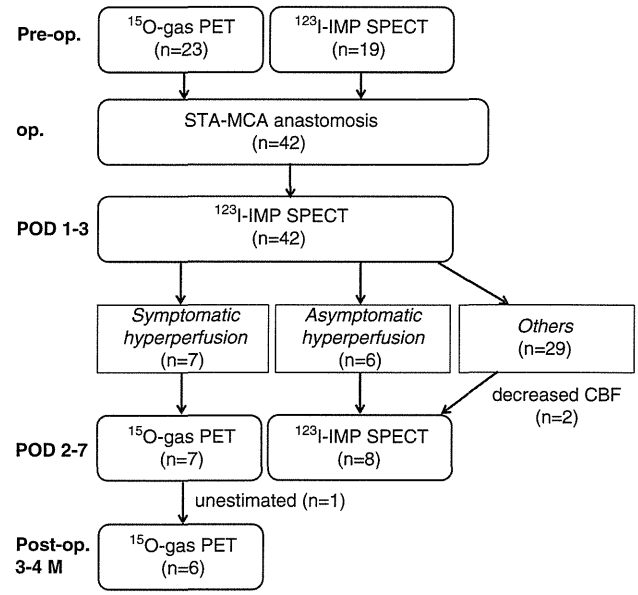

Figure 1 The protocol of the examination. As for screening, ^{123}I-IMP SPECT was conducted first during postoperative day (POD) 1 to 3 for all patients to determine qualitatively the presence of a significant focal increase in cerebral blood flow (CBF) at the site of anastomosis. Then, if patients with hyperperfusion on postoperative ^{123}I-IMP SPECT developed focal neurologic deficits, they underwent the PET study on POD 2 to 7. If patients did not develop new apparent neurologic symptoms despite hyperperfusion on ^{123}I-IMP SPECT, then they were classified as asymptomatic hyperperfusion and repeated the ^{123}I-IMP SPECT study during the subacute stages. Patients with symptomatic hyperperfusion repeated the PET study during the chronic phase 3 to 4 months after surgery. ^{123}I-IMP, ^{123}I-iodoamphetamine; SPECT, single-photon emission computed tomography; PET, positron emission tomography; STA-MCA, superficial temporal artery-middle cerebral artery.

infarction on postoperative diffusion-weighted magnetic resonance (MR) imaging were excluded. Patient with a significant focal increase in CBF at the site of anastomosis on ^{123}I-IMP SPECT were diagnosed as hyperperfusion, as reported previously (Fujimura *et al*, 2007, 2011). Then, if the patients with hyperperfusion on postoperative ^{123}I-IMP SPECT developed focal neurologic deficits related to the perisylvian area (dysarthria, hand motor dysfunction, and motor or sensory dysphasia) and/or severe headache (symptomatic hyperperfusion), they underwent CBF and metabolism measurements with PET during the subacute stage on POD 2 to 7. If patients did not develop new apparent neurologic symptoms despite hyperperfusion on ^{123}I-IMP SPECT, then they were classified as asymptomatic hyperperfusion and repeated the ^{123}I-IMP SPECT study during the subacute stages. The rest of the patients without apparent hyperperfusion on ^{123}I-IMP SPECT did not repeat the ^{123}I-IMP SPECT study unless there was a significant decrease in CBF. Patients with symptomatic hyperperfusion repeated the PET study during the chronic phase 3 to 4 months after surgery. Relative increases in and absolute values of CBF in PET during symptomatic hyperperfusion in MMD were compared with those of the traditional definition of post CEA hyperperfusion (>100% increase

over preoperative CBF values) and the predefined CBF value as normal control + 2s.d.

Positron Emission Tomography Measurement

A series of PET scans were performed to quantitatively assess CBF and cerebral metabolic rate of oxygen ($CMRO_2$) at each stage, according to the dual-tracer autoradiographic protocol developed by Kudomi *et al* (2005) with a minor modification of replacing intravenous administration of ^{15}O-water by ^{15}O-carbondioxide inhalation (Nezu *et al*, 2012). The PET scanner used was ECAT ACCEL from Siemens-CTI (Knoxville, TN, USA), and data were acquired in the 2D mode. The scan can provide an intrinsic spatial resolution of 4.5 mm full-width at half-maximum at the center of the field-of-view. A catheter was placed in the brachial artery for measurement of arterial input function. After a 10-minute transmission scan using a rotating external ^{68}Ge-^{68}Ga rod source, a PET scan was obtained 3 minutes after inhalation of ^{15}O-labeled carbon monoxide gas ($C^{15}O$) of 2,500 MBq for 30 seconds. After the 10 minutes allotted for radioactivity decay, an additional dynamic scan was performed for 8 minutes, while 4,000 MBq of oxygen ($^{15}O_2$) and 5,000 MBq of ^{15}O-labeled carbon dioxide ($C^{15}O_2$) were inhaled through a facemask sequentially at 5-minute intervals. The inhalation period was 1 minute for each gas. Arterial blood was continuously withdrawn during this dynamic scan, and the radioactivity concentration of the blood in the catheter tube was monitored using a scintillator block detector system (BeCON; Molecular Imaging Lab Inc., Suita City, Japan) (Kudomi *et al*, 2003). Arterial blood samples were also taken before and after the dynamic scan, and arterial oxygen content (PO_2) and arterial PCO_2 were measured.

Control values of PET parameters were obtained from eight patients (six male and two female; mean age ± s.d. = 66.1 ± 9.4 years) who had unilateral stenosis of the internal carotid artery or the trunk of MCA with minimal or no infarction on magnetic resonance imaging. Values of PET parameters obtained from the contralateral MCA region were as follows: CBF, 46.6 ± 5.6 mL/100 g per minute; cerebral blood volume (CBV), 2.90 ± 0.61 mL/100 g; $CMRO_2$, 3.56 ± 0.62 mL/100 g per minute; oxygen extraction fraction (OEF), 0.43 ± 0.05; and CBF/CBV, 18.8 ± 6.8/min. There were no significant changes in these values with advancing age.

Single-Photon Emission Computed Tomography Measurement

Preoperative clinical SPECT studies followed the DTARG protocol, with dual administration of iodoamphetamine (Kim *et al*, 2006). Briefly, two dynamic scans were acquired in quick succession, with a 2-minute interval between scans. The first scan covered the initial 0- to 28-minute period and the second was acquired from 30 to 58 minutes. At 4 minutes per frame, seven frames covered each of the two dynamic scan periods. ^{123}I-Iodoamphetamine was infused twice over 1 minute into the antecubital vein at 0 and 30 minutes. Acetazolamide (17 mg/kg, 1,000 mg maximum) was administered intravenously 20 minutes after the first iodoamphetamine injection, corresponding to 10 minutes before the second iodoamphetamine injection. Projection data were summed for the acquisition duration of the first and second scans and reconstructed. The SPECT data provide quantitative information on CBF at rest and after an acetazolamide challenge; it provides information about vascular reserve and the severity of hemodynamic brain ischemia. Regional vascular reserve was defined as the ratio of the difference between acetazolamide-activated regional CBF (rCBF) and resting rCBF to resting rCBF: Regional vascular reserve = ((acetazolamide-activated rCBF/resting rCBF − 1) × 100(%)). The severity of hemodynamic brain ischemia was classified into three stages as follows: stage 0 (vascular reserve > 30%), stage I (30% ⩽ vascular reserve ⩽ 10% or 80% of normal CBF ⩽ resting CBF), and stage II (10% > vascular reserve > −30% and 80% of normal CBF > resting CBF) (JET study Group, 2002). This classification was based on hemodynamic status, determined from PET findings (Powers, 1991). The ^{123}I-IMP autoradiographic method (Iida *et al*, 1994) was performed postoperatively for all patients. The ^{123}I-IMP autoradiographic method uses a single iodoamphetamine administration to assess CBF at rest. The same image reconstruction process as for the DTARG protocol was used.

Magnetic Resonance Imaging Protocol

The MR imaging was performed using a 1.5-T MR scanner (Symphony, Siemens, Erlangen, Germany) fitted with a circularly polarized head coil. Fast fluid-attenuated inversion recovery MR images were acquired before STA-MCA anastomosis (7 ± 5 days before or after the first PET). Sequence parameters were as follows: repetition time/echo time/number of excitations, 9,000 ms/120 ms/1; inversion time, 2,500 ms; turbo factor, 15; and matrix, 352 × 352. Additional MR scans were also performed on each patient during the hyperperfusion phase (1 ± 2 days before or after the second PET) and the chronic phase (7 ± 5 days before or after the third PET).

Data Analysis

The PET images were reconstructed using a standard filtered-back projection technique on the PET scanner console, which included corrections for a scatter and attenuation. A postreconstruction Gaussian filter of 8 mm full-width at half-maximum was also applied. All PET and MR images were then transferred to an independent PC workstation for further analyses. Functional images for CBF, $CMRO_2$, OEF, and CBV were obtained using an in-house program published previously (Kudomi *et al*, 2005), with a minor modification in the process of compensating for the recirculation water in the arterial blood (Iida *et al*, 1993) with automatic separation of two input functions (Kudomi *et al*, 2009). All PET images were registered to the CBF image taken at the preoperative study using Multimodality Image Registration Software (Dr View, AJS Inc., Tokyo, Japan), which fits six rigid body parameters using a mutual information matching technique. The MR images taken at three different time points

were also registered to the CBF image so that all PET and MR images were aligned at the same coordinates. Agreement of the registered images was visually confirmed to match the brain contours between PET and MR images, including the cerebellum, sylvian fissure, and ventricular regions.

Regions-of-interest were carefully selected using QView software from the QSPECT project at National Cerebral and Cardiovascular Center Research Institute (Osaka, Japan) (Iida *et al*, 2010). For quantitative assessment of CBF, $CMRO_2$, OEF, and CBV using PET in patients with symptomatic hyperperfusion, regions-of-interest were constructed to delineate areas of increased CBF around the site of anastomosis on the postoperative PET during the subacute stage compared with preoperative CBF images on PET/SPECT. Regions-of-interest were then superimposed on other PET and MR images. For the rest of the patients in whom preoperative PET was performed, regions-of-interest, consisting of a 1-cm diameter circle along the cortical rim, avoiding the infarcted area, were manually placed over the frontal cortex (targeted to the central area where anastomosis was planned).

Statistical Analysis

All data are presented as the mean ± s.d. All data were analyzed by analysis of variance. If significance was obtained, then we used Scheffe's criteria for multiple comparison. $P<0.05$ was considered to be significant.

Results

Clinical Characteristics

Preoperative hemodynamic status was categorized using PET and SPECT in 23 (9 sides at stage I and 14 sides at stage II) and 19 (9 sides at stage I and 10 sides at stage II) hemispheres in 34 patients, respectively. In the qualitative ^{123}I-IMP SPECT study on POD 1 to 3, a significant focal increase in CBF at the site of anastomosis was observed in 13 sides (31%), whereas decreased CBF was noted in 2 sides (4.8%). Of the patients with hyperperfusion on qualitative ^{123}I-IMP SPECT, seven sides (16.7%) in six patients became symptomatic (symptomatic hyperperfusion) and subsequently underwent the PET study during POD 2 to 7. The rest of the study population were classified as asymptomatic hyperperfusion in 6 sides (14.3%) and others in 29 sides (69%) based on qualitative ^{123}I-IMP SPECT and the appearance of postoperative new neurologic symptoms (the traditional definition of postoperative hyperperfusion in MMD).

Table 1 presents a summary of the cases with symptomatic hyperperfusion. All patients complicated with symptomatic hyperperfusion presented with ischemic attacks. The incidence of symptomatic hyperperfusion was correlated with the degree of preoperative hemodynamic impairment; 5.9% (1 of 18 sides) at stage I and 25.0% (6 of 24 sides) at stage II. Hyperperfusion on the PET scan was observed in the area near the site of STA-MCA anastomosis. Symptoms related to hyperperfusion included seizure, sensory disturbance, and aphasia in three, two, and two cases, respectively. Symptoms occurred on POD 1 to 4, with the duration being 4 to 14 days. The modified Rankin scale score of patients complicated with symptomatic hyperperfusion was 0 or 1 at postoperative months 3 to 4.

Correlation of Preoperative Positron Emission Tomography Parameters with Symptomatic Hyperperfusion

Table 2 presents preoperative PET parameters in 22 hemispheres of 18 patients. One patient with postoperative decreased CBF on qualitative ^{123}I-IMP SPECT was excluded. These hemispheres were

Table 1 Summary of seven cases in six patients with postoperative symptomatic hyperperfusion

Case no.	*Age, sex*	*Side*	*Onset of MMD*	*Preoperative hemodynamic status*	*Area of hyperperfusion*	*Symptom*	*Onset of hyperperfusion*	*Duration (days)*	*mRS score at 3–4 months*
1	41, F	L	Infarction	Stage II	Precentral and central	Seizure	POD 0	10	1
2	37, M	R	TIA	Stage I[a]	Central and parietal	Seizure	POD 4	4	0
3	44, F	L	Infarction	Stage II	Central	Seizure	POD 3	7	1[b]
4	44, F	R	Infarction	Stage II	Central	Sensory	POD 3	11	1[b]
5	41, F	R	TIA	Stage II	Central	Sensory	POD 3	7	0
6	60, F	L	Infarction	Stage II	Precentral and central	Aphasia	POD 1	11	0
7	51, M	L	TIA	Stage II[a]	Precentral, central, and parietal	Aphasia	POD 3	14	0

^{123}I-IMP, ^{123}I-iodoamphetamine; MMD, moyamoya disease; mRS, modified Rankin Scale; POD, postoperative day; sensory, sensory disturbance; SPECT, single-photon emission computed tomography; TIA, transient ischemic attack.
Case no. 3 and no. 4 were the same patient.
[a]Evaluated by ^{123}I-IMP SPECT.
[b]Resulted from infarction that occurred at the onset of MMD.

Table 2 Preoperative PET parameters in 22 hemispheres of 18 patients

	Postoperative hyperperfusion			P *value*
	Symptomatic	*Asymptomatic*	*Others*	
n	5	4	13	
CBF (mL/100 g per minute)	34.1 ± 8.2	43.2 ± 8.2	33.5 ± 8.8	0.202
CBV (100 g/min)	5.77 ± 1.67	4.63 ± 0.29	4.49 ± 1.06	0.166
$CMRO_2$ (mL/100 g per minute)	3.48 ± 0.51	3.07 ± 0.41	2.92 ± 0.64	0.253
OEF	0.61 ± 0.09	0.44 ± 0.10	0.51 ± 0.08	0.045
CBF/CBV (per minute)	6.7 ± 2.2	9.5 ± 1.6	8.3 ± 2.4	0.236

CBF, cerebral blood flow; CBV, cerebral blood volume; $CMRO_2$, cerebral metabolic rate of oxygen; OEF, oxygen extraction fraction; PET, positron emission tomography.
Values are mean ± s.d.

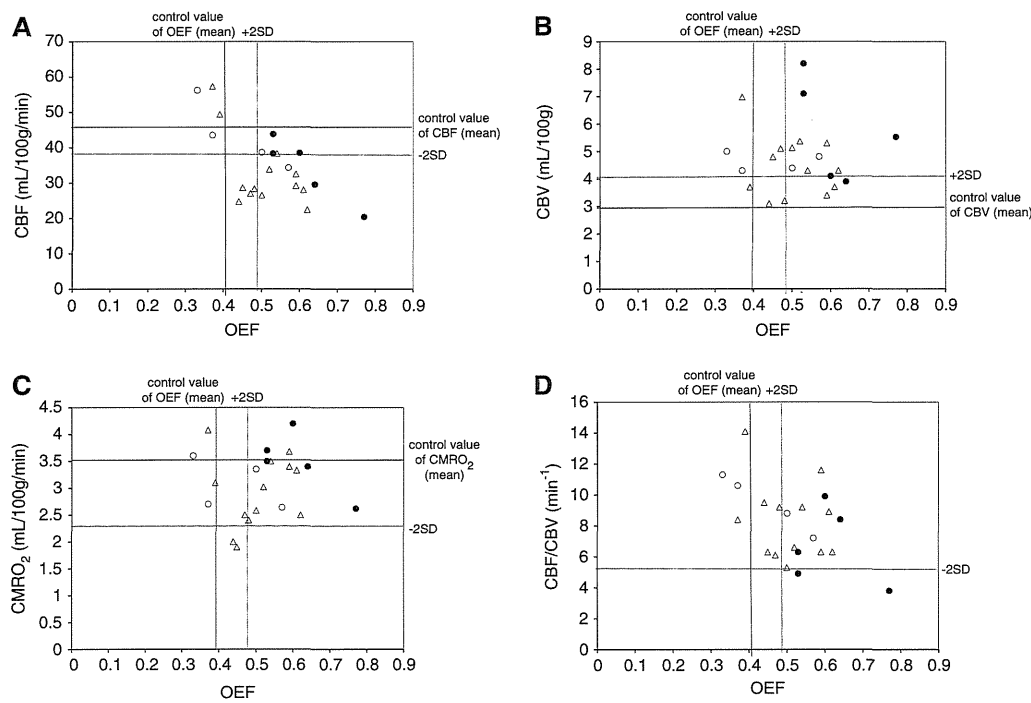

Figure 2 Plot of preoperative absolute values of oxygen extraction fraction (OEF) versus cerebral blood flow (CBF) (**A**), cerebral blood volume (CBV) (**B**), cerebral metabolic rate of oxygen ($CMRO_2$) (**C**), and CBF/CBV (**D**) in 22 hemispheres of 18 patients. Patients were divided by postoperative qualitative ^{123}I-IMP SPECT into three groups: symptomatic hyperperfusion (filled circle), asymptomatic hyperperfusion (open circle), and others (triangle). Solid vertical and horizontal black lines indicate control values of positron emission tomography (PET) parameters and the dotted lines indicate ± 2s.d. for control values of PET parameters, respectively. Four of eight cases with increased OEF and CBV (**B**, upper right quadrant) had postoperative symptomatic hyperperfusion. ^{123}I-IMP, ^{123}I-iodoamphetamine; SPECT, single-photon emission computed tomography.

divided into symptomatic hyperperfusion ($n=5$), asymptomatic hyperperfusion ($n=4$), and others ($n=13$). Although no significant differences in CBF, CBV, $CMRO_2$, and CBF/CBV were found between the three groups, OEF of the hemisphere complicated with symptomatic hyperperfusion was significantly higher than that of the other two groups ($P<0.05$). Relationships between OEF and CBF, CBV, $CMRO_2$, or CBF/CBV were shown in Figure 2. Cases complicated with symptomatic hyperperfusion were almost exclusively noted in those with increased OEF. Of note, four of eight cases (50%) with increased OEF and CBV (Figure 2B, upper right quadrant) had postoperative symptomatic hyperperfusion.

Postoperative Positron Emission Tomography Parameters in Symptomatic Hyperperfusion

Figure 3 illustrates temporal changes in PET parameters in seven hemispheres of six patients with postoperative hyperperfusion. The CBF values in patients with postoperative hyperperfusion significantly increased from the preoperative baseline value of 34.1 ± 8.2 mL/100 g per minute ($n=5$) to